

Turbulent Transport of Dust Particles in Protostellar Disks: The Effect of Upstream Diffusion

TING-TAO ZHOU(周廷骏),¹ HONG-PING DENG(邓洪平),² YI-XIAN CHEN(陈逸贤),³ AND DOUGLAS N. C. LIN(林潮)^{4,5}

¹*Department of Mechanical and Civil Engineering, California Institute of Technology, Pasadena, CA 91125, USA*

²*Shanghai Astronomical Observatory, Chinese Academy of Sciences, Shanghai 200030, China*

³*Department of Astrophysics, Princeton University*

⁴*Department of Astronomy & Astrophysics, University of California, Santa Cruz, CA 95064, USA*

⁵*Institute for Advanced Studies, Tsinghua University, Beijing 100086, China*

ABSTRACT

We study the long-term radial transport of micron to mm-size grain in protostellar disks (PSDs) based on diffusion and viscosity coefficients measured from 3D global stratified-disk simulations with a Lagrangian hydrodynamic method. While gas-drag tend to transport dust species radially inwards, stochastic diffusion can spread a considerable fraction of dust radially outwards (upstream) depending on the nature of turbulence. In gravitationally unstable disks, we measure a high radial diffusion coefficient $D_r \sim H^2\Omega$ with little dependence on altitude. This leads to strong and vertically homogeneous upstream diffusion in early PSDs. In the solar nebula, the robust upstream diffusion of μm to mm size grains not only efficiently transports highly refractory μm -size grains (such as those identified in the samples of comet 81P/Wild 2) from their regions of formation inside the snow line out to the Kuiper Belt, but can also spread mm-size CAI formed in the stellar proximity to distances where they can be assimilated into chondritic meteorites. In disks dominated by magnetorotational instability (MRI), the upstream diffusion effect is generally milder, with a separating feature due to diffusion being stronger in the surface layer than the midplane. This variation becomes much more pronounced if we additionally consider a quiescent midplane with lower turbulence and larger characteristic dust size due to non-ideal MHD effects. This segregation scenario helps to account for dichotomy of two dust populations' spatial distribution as observed in scattered light and ALMA images.

1. INTRODUCTION

The omnipresence of protostellar disks (PSDs) (Hartmann 1998) provides birth sites and incubators for emergence of planets (Cameron 1978; Hayashi et al. 1985; Lin & Papaloizou 1985; Ida & Lin 2004). The temperature distribution in these disks inferred from their observed spectral energy distribution (Adams et al. 1987; Hartmann 1998) matches well with those from theoretical thermal equilibrium models where the cooling rate from the disk surface is balanced by both intrinsic viscous dissipation and stellar irradiation (Chiang & Goldreich 1997; Garaud & Lin 2007). This provides a natural division for the condensation sequence of terrestrial, asteroids, gas and ice giant planets (Ruden & Lin 1986).

In such a setting, refractory and volatile grains are expected to condense in the stellar proximity (within ~ 0.1 au) and outside the snow line (several aus) respectively. Yet, μm -size crystalline refractory grains are found in abundance among the Stardust return samples from comet 81P/Wild 2 (Brownlee et al. 2006). Their presence is also inferred from the IR spectra of other comets (Wooden et al. 2007) as well as extended regions

(out to ~ 10 au) of PSDs (Bouwman et al. 2003, 2008; van Boekel et al. 2005; Watson et al. 2009).

The crystalline structure requires the melt-down and re-condensation of amorphous silicate grains at temperatures $\gtrsim 1000\text{K}$, depending on composition (Bockelée-Morvan et al. 2002), while their implantation into comets occurs below the icy condensation temperature $\lesssim 160\text{K}$. Therefore, very efficient mechanisms need to be invoked for these grains to be transported outwards after re-condensation in the stellar proximity. Explanations for this thermal paradox include large scale diffusion (Morfill & Voelk 1984; Clarke & Pringle 1988), spreading of the solar nebula (Safronov & Ruzmaikina 1985; Ciesla 2007), meridional circulation (Urpin 1984; Kley & Lin 1992), radiation-pressure driven outflow in the disk surface (Takeuchi & Lin 2003), fluctuating X-wind (Shu et al. 2000, 2001; Shang et al. 2000), and shock heating (Weidenschilling et al. 1998; Wooden et al. 2007; Desch et al. 2012; Gong et al. 2019).

Optical and NIR maps of scattered light also indicate that in certain PSDs, the micron-size particles have larger radial extent and thickness than those of larger

mm-size particles inferred from ALMA images of reprocessed radiation (Villenave et al. 2020; Benisty et al. 2022). This suggests that dust of different characteristic size, occupying different vertical layers of the disk, may have distinct capabilities of radial transport.

In this paper, we revisit the diffusion hypothesis. The structure and evolution of PSDs including the solar nebula are regulated by turbulent viscosity. Some causes of turbulence include the magneto-rotational instability (MRI) (Balbus & Hawley 1991) and gravitational instability (GI) (Safronov 1960; Toomre 1964) in non-magnetised (see, e.g., Durisen et al. 2007) and magnetised disks (Riols & Latter 2019; Deng et al. 2020). The chaotic turbulent motion is correlated and leads to Reynold and Maxwell stress and effective torque which transport gas angular momentum outwards, while inducing mass spreading (Pringle 1981; Balbus & Hawley 1998) and diffusion of passive contaminants including small grains (Morfill & Voelk 1984; Clarke & Pringle 1988)¹ A key issue is whether turbulent diffusion of crystalline grains or heavy-element tracers can diffuse against the inward gas flow and spread widely over extended regions of the disk. We present in §2 three sets of numerical simulation for MRI, GI in the absence of magnetic fields (GI-HD), and GI of disks with magnetic fields (GI-MHD). Based on measurements from state-of-the-art simulations in §3, we construct simplified 1D models of layered accretion disks and examine the global diffusion process of dust elements in turbulent disks in §4, focusing on the evolution of their concentration distribution. In §5, we summarize our results and discuss their implications.

2. SIMULATIONS AND ANALYSIS

The simulations of GI-HD, MRI and GI-MHD turbulence are drawn from Deng et al. (2020) dedicated to studying the interplay between magnetic fields and spiral density waves. The simulations were carried out with a Godunov-type Lagrangian method, the meshless finite mass (MFM) method in the GIZMO code² (Hopkins 2015) which shows excellent conservation property in GI disk simulations (Deng et al. 2017). At sufficiently high resolution, MFM can also capture the MRI and the ensuing turbulence showing good agreement with grid-code simulations (Deng et al. 2019, 2020). In all the sim-

ulations, the disk mass is about 0.07 the stellar mass and the disk is resolved by $> 35M$ particles/elements, i.e., a Jupiter mass object is resolved by half a million computational elements, among the highest resolution GI disk simulations.³ The initial surface density is inversely proportional to the radius spanning 5–25 au. The code units are 1 au, 1 solar mass and $G = 1$.

In the following analysis, the MRI and GI-MHD turbulence corresponds to the model MRI-hr and grvmhd1 simulation. We then turn off the magnetic fields in the grvmhd1 model and run it for 400 additional years and this simulation is named grvhd1 here. We show representative mid-plane density maps⁴ in the quasi-steady state in Figure 1. The MRI turbulence is mild with small density contrast while GI turbulence, regardless of the presence of magnetic fields, show strong density fluctuations. The flocculent spirals in the grvmhd1 model become more coherent after turning off the magnetic fields and saturating to grvhd1 resembling previous hydrodynamic simulations of gravitational instability (Deng et al. 2017; Béthune et al. 2021). This in turn confirmed the important back reaction of magnetic fields on the spiral density wave morphology (for details, see Deng et al. 2020).

In the well-coupled regime, dusts are tied to the Lagrangian fluid elements so that we can directly analyse the fluid elements' trajectories to uncover particle motions. This is different from injecting and analysing tracers of different sizes into either Lagrangian (Rice et al. 2004) or Eulerian hydrodynamic simulations (Haghighipour & Boss 2003; Boley & Durisen 2010; Zhu et al. 2015; Riols et al. 2020b; Baehr & Zhu 2021; Hu & Bai 2021). To our knowledge, this work amounts to be the first study of fluid tracers in global Lagrangian simulations of magnetised/self-gravitating accretion discs.

We trace fluid elements in the quasi-equilibrium turbulence for 250 years (two rotation periods at 25 au), which is sufficient to identify the particles diffusion coefficients. We choose particles in small annuli centered at 10 au and 12.5 au with a width of 0.001 au. In each annulus, there are more than 2000 particles. For ex-

¹ An analogous turbulent-diffusion mechanism has also been invoked to account for the shallow abundance gradient in disk galaxies (Clarke 1989; Yang & Krumholz 2012; Krumholz et al. 2018).

² The code is publicly available at <http://www.tapir.caltech.edu/~phopkins/Site/GIZMO.html>.

³ We note that thanks to the adaptive nature of Lagrangian methods, even a 1M particle simulation produces converged results comparable to some ultra-high resolution grid-code simulations (up to 2 billion effective cells) in GI disk modeling. See the Wengen code comparison project test4, including one Lagrangian code, Gasoline and four grid codes (some of which with mesh refinement), Enzo, FLASH, CHYMER and IU code at <http://users.camk.edu.pl/gawrysz/test4/>.

⁴ This is similar to the mid-row of figure 2 in Deng et al. (2020) and the high density inner edge in that figure is due to artificial effects during plotting.

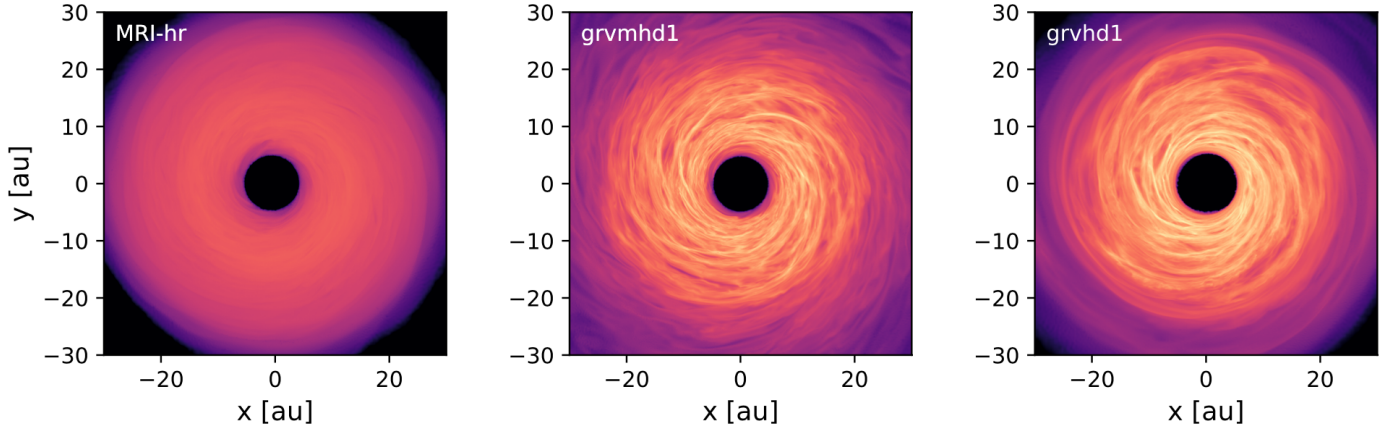


Figure 1. The mid-plane volume density in quasi-equilibrium turbulence of MRI, GI-MHD and GI-HD simulations. The colors, from black to yellow, show the density ranging from 10^{-15} to 10^{-9} g/cm $^{-3}$ in a logarithmic scale.

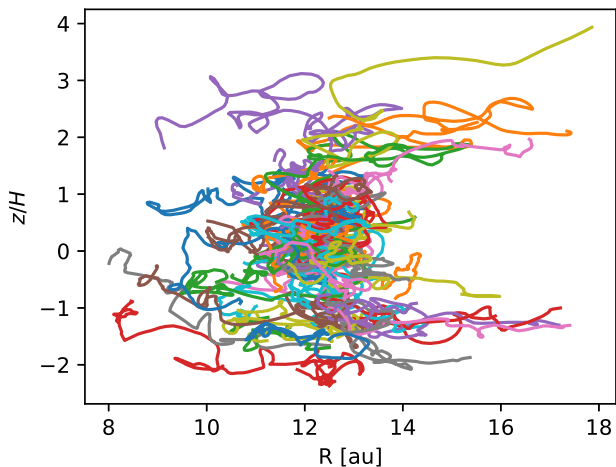


Figure 2. The trajectories of particles in the MRI simulation ($R - z$ plane) initially at 12.5 au within five local orbits.

ample, we follow the trajectories of fluid elements in a narrow annulus of width 0.001 au in the MRI-hr simulation and plot the trajectories of 100 randomly chosen particles out of the >2000 particles in Figure 2.

The three simulations have distinct thermophysics and vertical structures (see, Figure 2 of Deng et al. 2020) and thus, for ease in comparison, we need to normalise the statistics to an appropriate length scale. Specifically, the MRI-hr simulation is adiabatic and the accretion heats up the disk gradually; the grvmhd1 and grvhd1 saturates to a state where the heating is balanced by a prescribed cooling at a rate of the orbital periods (Deng et al. 2020). In addition, the disk vertical structure is strongly fluctuating the GI simulations so that the traditional definition of the vertical scale-height is not adequate.

We adopt the dynamic scale-height (H) definition of Ogilvie (2018) where H is the square root of the second vertical moment of the density field, i.e.,

$$H = \sqrt{\frac{\int \rho z^2 dz}{\int \rho dz}}. \quad (1)$$

It naturally reduce to the ratio between the speed of the sound (c_s) and the local rotational frequency (Ω) for a vertical Gaussian profile. We take the time (250 years) and azimuthal average the dynamic scale-heights for the three simulations and show them in Figure 3.

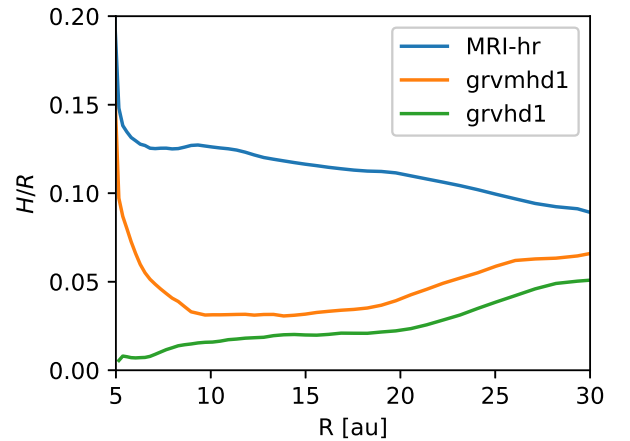


Figure 3. The averaged dynamic scale height in the quasi-equilibrium turbulence.

The adiabatic MRI-hr simulation is hot with a typical $H/R = 0.1$ (due to the initial condition). The inner disc is relatively hotter due to a faster development (small Ω^{-1}) of MRI turbulence than the outer region in the adiabatic simulation. The grvmhd1 and grvhd1 have

significantly thinner/colder discs with H/R around 0.03 and 0.02. In further analysis, we normalise displacements to H to enable comparison across different models and with previous grid-code simulations (Zhu et al. 2015; Riols et al. 2020b). However, for simplicity, a thermal profile with constant H/R is adopted for GI, GI-MHD and MRI in the simplified 1-D dust transport model in §4.

Runaway types of super-diffusion processes have been reported for certain highly supersonic turbulence, in which there is no well-defined diffusion coefficient (Colbrook et al. 2017). In contrast, our global simulations corroborate with previous local simulations (Zhu et al. 2015; Shi et al. 2016) to show that GI and MRI, as turbulence typically on the sonic level (characteristic length scale comparable to H), induce regular Gaussian/Brownian diffusion of passive tracers. We can measure diffusion coefficients through the displacement of these tracers (see Figure 2), as elaborated in §3. Our approach is similar to the method applied in grid-code simulations to measure the diffusion coefficients of Lagrangian particles with finite Stokes number T_S . As we mentioned, since particles represent gas itself in our simulations, we directly measure the diffusion coefficients of passive particles well-coupled with gas (the limit of small $T_S \rightarrow 0$), however, diffusivity measured in this limit are proven to be valid for small dust Stokes number up to $T_S \lesssim 0.1$ (Zhu et al. 2015; Shi et al. 2016), consistent with analytical scaling from Youdin & Lithwick (2007).

The measured relevant diffusion coefficient discussed below are summarised in Table 1. Although $D \sim \alpha H^2 \Omega$ is often applied in grid-based dust-gas hydrodynamic simulations (Zhu et al. 2011; Zhu et al. 2012; Chen et al. 2021), we show that this approximation can be off by up to an order of magnitude. D_r is the overall radial diffusion coefficient and D_z is the overall vertical diffusion coefficient. To explore possibility of layered radial diffusion, we also divide disks into the disk midplane within $|z| < H$ and the disk atmosphere $|z| > H$, and measure the radial diffusion coefficients D_{mid} and D_{sur} for each layer. We generally expect that with a large D_z , the vertical mixing of dust/gas at different altitudes becomes very efficient such that $D_{\text{mid}} \sim D_{\text{sur}}$ whereas they may differ more significantly when D_z is small.

3. DUST DIFFUSION IN REAL TURBULENCE

3.1. gravitationally unstable disks

Young circumstellar disks are relatively massive to their hosts and can be unstable due to gas self-gravity forming spiral density waves (see, e.g. reviews by Durisen et al. 2007; Kratter & Lodato 2016). The spiral

Table 1. dust diffusion coefficients

Run	Physics	D_r	D_{mid}	D_{sur}	D_z	α
grvhd1	GI	2.	1.9	2.1	0.2	0.1
grvmhd1	GI-MHD	0.5	0.49	0.5	0.1	0.23
MRI-hr	MHD	0.045	0.033	0.07	0.013	0.02

Table 1. The diffusion coefficients (given in a unit of $H^2 \Omega$) by linear regression of the dust mean squared displacement (MSD). Note, for self-gravitating disk, only the early stage vertical MSD evolution reflects the fast vertical motion (see text). Here D_{mid} and D_{sur} are measured dust radial diffusion coefficients for particles with initial position $|z| < H$ and $|z| > H$, respectively. In the unit of $H^2 \Omega$, ν corresponds to the value of α in the widely adopted α prescription for effective viscosity Shakura & Sunyaev (1973), and D/ν are referred to as Schmidt numbers. We see that while radial D_r/ν span a wide range, the vertical D_z/ν are always of order-unity. Schmidt numbers are also sometimes used to refer to the ratio between dust diffusivity and gas diffusivity, which we assume to be 1 in this study for small T_S (Youdin & Lithwick 2007). We will not be using this term in the rest of this paper to avoid confusion.

density waves are critical for angular momentum transport and thus disk accretion. The spiral density wave also excites strong vertical circulation and likely powers a large scale dynamo amplifying any weak magnetic fields to near thermal strength (Riols & Latter 2019; Deng et al. 2020; Löhner & Peeters 2022). The strong fields facilitates accretion in early discs significantly and may impact the population of planet formed via disk instability (Deng et al. 2021).

In an gravitationally unstable disks, the vertical circulation (Boley & Durisen 2006; Deng et al. 2020) besides spirals efficiently mixes small particles at different altitudes above the disk mid-plane in local shearing box simulations (Riols et al. 2020b; Baehr & Zhu 2021). In order to characterize the difference in turbulent diffusion in disks regulated by MRI and GI, we plot the vertical motion of 15 randomly chosen particles in the annulus centered at 12.5 au in Figure 4. Particles in the MRI turbulence show minor vertical motion (model MRI-hr), implying a slow vertical diffusion. This weak coupling also enables particles in the disk mid-plane and surface to diffuse at different rates. In contrast, the vertical motion over a dynamical time scale extend to the scale of H in GI turbulence (models grvmhd1 and grvhd1). This random motion leads to efficient particle exchanges in the vertical direction and inhibits a significant differential radial diffusion between the disk mid-plane and surface.

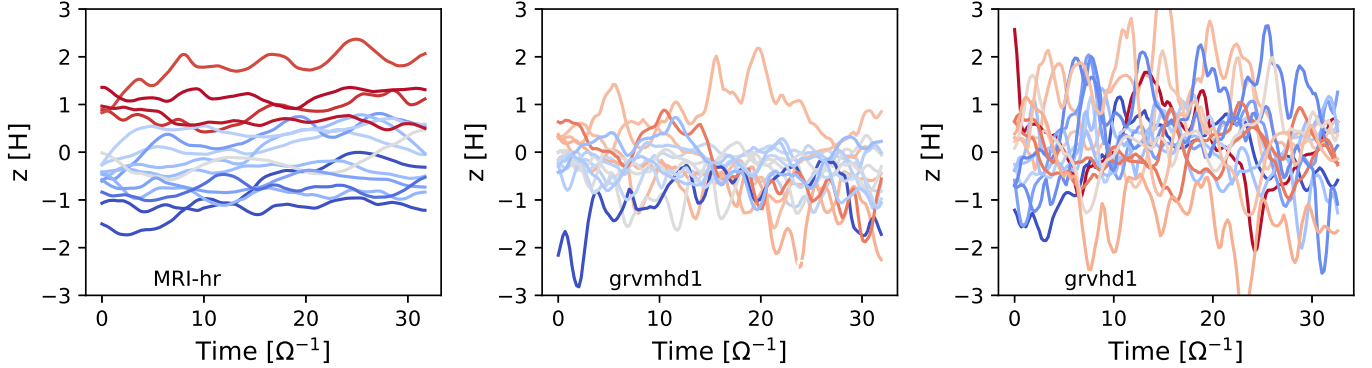


Figure 4. The vertical motion of randomly chosen particles in the annuli centered at 12.5 au. .

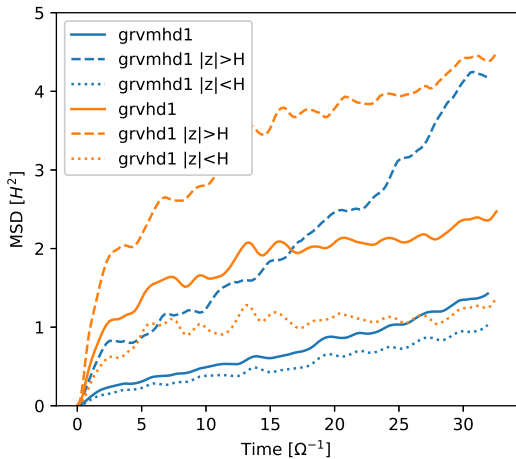


Figure 5. The evolution (given in units of the local dynamical time) of the mean squared displacement along the vertical direction for particles in annuli centered at 12.5 au initially. Here the MSD is normalised to the dynamical scale-height at 12.5 au. .

The vertical diffusion process in grvmhd1 and grvhd1 can be quantified by the vertical mean-squared displacement (MSD). In Figure 5, we plot the averaged vertical MSD for particles in the disk mid-plane ($|z| < H$) and surface ($|z| > H$) versus the all-particle average MSD around 12.5 au, as functions of diffusing time. In both grvmhd1 and grvhd1, the vertical MSD experience a fast increase followed by a slower but steady growth. We measure a mean vertical diffusion rate of $D_z = 0.2H^2\Omega$ and $0.1H^2\Omega$ for the grvhd1 and grvmhd1, comparable to their viscosity $\nu = \alpha H^2\Omega = 0.1H^2\Omega$ and $0.23H^2\Omega$ (Deng et al. 2020), also summarised in Table 1. After the particles in the narrow annulus (initially confined) spreads out along a large scale eddy, the growth of vertical MSD become slow in grvmhd1 or negligible in grvhd1. The initial fast increase in MSD is typical for high altitude particles ($|z| > H$), suggesting faster flow

in the disk surface layer (dashed lines). However, over a few dynamical timescales the MSD growth quickly saturate towards a lower pace that converges with the average diffusion rate (dotted lines), since particles' movement is hindered by their rapid circulation across lower altitudes ($|z| \sim H$), where diffusion is much slower. In principle, we can measure somewhat different vertical diffusion coefficients $D_{z,mid} \ll D_{z,sur}$ from the initial trend of dashed and dotted lines in Figure 5. Nevertheless, since vertical mixing is efficient suggesting particles commute across different layers frequently (as shown in Figure 4), it would be more meaningful to simply apply the average diffusion coefficient in following discussions for disks with gravitational instability.

Moreover, due to efficient vertical mixing, the radial MSD shows little altitude dependence $D_r \approx D_{mid} \approx D_{sur}$. As a result, we only plot the average all-particle MSD (used to measure D_r) for all particles centered at 10 au and 12.5 au in Figure 6. At the two different radii, the MSD evolves similarly so that our results apply to general GI and GI-MHD turbulence. Similar to the vertical MSD evolution, the radial MSD also increase rapidly at the early stage when the particles are moved around by the vertical circulation. However, particles can hop onto new eddies and be radially transported over large distances. As a result, the radial MSD continues to grow. In the grvmhd1 model, the radial diffusion rate is $D_r = 0.5H^2\Omega$, twice the viscosity. In the grvhd1 model, the radial diffusion rate is $2H^2\Omega$ which is much larger than its viscosity $0.1H^2\Omega$, as summarised in the first 2 rows of Table 1.

3.2. MRI turbulence

Magnetised accretion disks are prone to the MRI provided sufficient ionization (Balbus & Hawley 1991), which further leads to vigorous turbulence that transports angular momentum outwards enabling gas accretion. In ideal MHD simulations, MRI turbulence has a

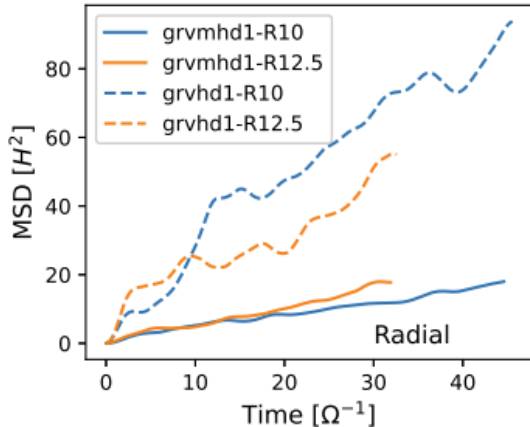


Figure 6. The evolution (given in units of the local dynamical time) of the mean squared displacement for particles. Here MSD is normalised to the dynamical scale-height at 12.5 au or 10 au. .

typical effective viscosity $\nu = \alpha H^2 \Omega$, with $\alpha \sim 0.02$ in grid-code (Simon et al. 2012; Beckwith et al. 2011) as well as Lagrangian simulations (Deng et al. 2019, 2020; Wissing et al. 2022). However, realistic PSDs are poorly ionized so that only the surface layer may be MRI active and turbulent or the whole vertical extent is laminar with winds launched at high altitude (Gammie 1996; Okuzumi & Hirose 2011; Bai & Stone 2013; Riols et al. 2020a). In that case, the contrast between D_{sur} and D_{mid} would be even more pronounced. Our ideal MHD (active at all altitudes) model is admittedly oversimplified and it offers the most conservative illustration for the layered dust diffusion tendency in MRI turbulence.

In Figure 7, we plot the MSD evolution for all particles in the annulus centered at 12.5 au and particles initially in the disk body with $|z| < H$ and disk surface with $|z| > H$ separately. There are some 1700 and 600 particles in the disk body and surface respectively. By the end of the simulation about 200 particles crossed the $z = \pm H$ boundary. If we restrict our analysis to those particles confined in the same (mid-plane or surface) portion of the disk (see, e.g. Zhu et al. 2015), we would find almost identical results to those in Figure 7. The particles show a mild uniform vertical diffusion rate about $D_z = 0.013H^2\Omega$ which is smaller than the viscous α parameter in units of $H^2\Omega$. A similar analysis for the particles in an annulus centered at 10 au reveals a vertical diffusion rate about $0.017H^2\Omega$ close to α . However, in Table 1, we restrict ourselves to the reference value measured at 12.5 au since the latter is less likely affected by the inner boundary (see Figure 3).

In the MRI context, the diffusion rates start to show dependence on the vertical altitude. Particles in the disk

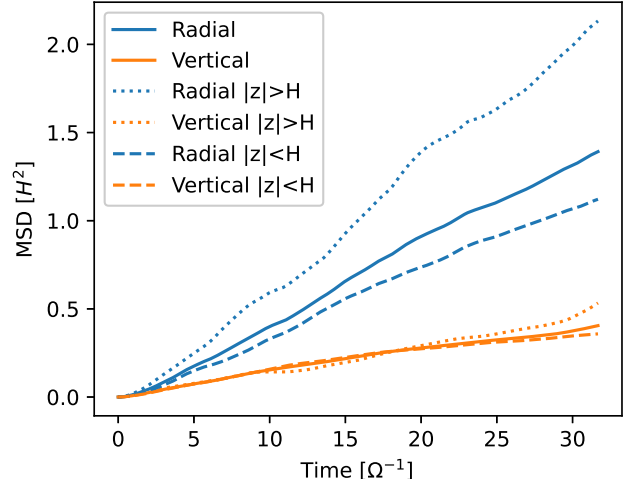


Figure 7. The evolution (given in units of the local dynamical time) of the mean squared displacement for particles initially at 12.5 au for the MRI-hr model. Here MSD is normalised to the dynamical scale-height at 12.5 au. .

mid-plane diffuse at a rate $D_{\text{mid}} = 0.033H^2\Omega$ whereas those at the disk surface diffuse at a faster rate of $D_{\text{sur}} = 0.07H^2\Omega$. This introduces a factor of two difference in their characteristic radial diffusion “velocity” $\sim D_r/R$. The analysis for particles centered at 10 au show similar radial diffusion rates within a few percent deviation.

Since both α and $D_z \approx \alpha$ are small, vertical mixing in the MRI-prone disks is much less efficient than the GI cases. Under such circumstance, the considerable difference between $D_{\text{mid}} < D_{\text{sur}}$ introduces potentials for a layered diffusion process. Moreover, to go beyond our ideal MHD simulation, in realistic disks the moderate turbulence rendering α and D_{sur} as measured in our simulations may only be active in the surface layer (Gammie 1996), while residue α and D_{mid} is much smaller in the dead zone below the atmosphere.

To study the long-term evolution of grain in fore-mentioned environments, we construct a 1D two-fluid disk model to further explore the long-term implications of the diffusion process with or without layered structure.

4. DUST TRANSPORT MODELS

In the case of GI or GI-MHD turbulence, the radial diffusion coefficients are similar and independent of the vertical position in the disk, as in Table 1. We write down the evolution for the dust concentration C , assuming cylindrical symmetry so that there will be no

explicit dependence on the azimuthal angle θ .

$$\Sigma \frac{\partial C}{\partial t} = \frac{1}{R} \frac{\partial}{\partial R} \left(RD\Sigma \frac{\partial C}{\partial R} \right) - \frac{1}{R} \frac{\partial}{\partial R} (R\Sigma v_d C) + C \frac{1}{R} \frac{\partial}{\partial R} (R\Sigma v_g) \quad (2)$$

$$\frac{\partial \Sigma}{\partial t} = \frac{3}{R} \frac{\partial}{\partial R} \left(R^{1/2} \frac{\partial}{\partial R} (\Sigma \nu R^{1/2}) \right) \quad (3)$$

where Σ is the gas density, C is the dust-to-gas surface density ratio, and Equation 3 describes the evolution of the gas density (Ruden & Lin 1986). In Equation 2 we generalize the formulation of Morfill & Voelk (1984); Clarke & Pringle (1988), where we include the radial velocities of dust v_d , which could differ from the radial velocity of the gas v_g . We note that the dust back reaction is often ignored in the gas nebula evolution (Equation 3) given the low dust concentration level of a few percent (see, e.g., Liu et al. 2022). The gas advective velocity in the radial direction follows (Lynden-Bell & Pringle 1974; Armitage 2019)

$$v_g = - \frac{3}{\Sigma R^{1/2}} \frac{\partial}{\partial R} (\nu \Sigma R^{1/2}) \quad (4)$$

$$= - \frac{3\nu}{R} \left(\frac{\partial \ln \Sigma}{\partial \ln R} + \frac{\partial \ln \nu}{\partial \ln R} + \frac{1}{2} \right). \quad (5)$$

For dust completely coupled with gas $v_d = v_g$, we can recover Equation 2.1.4 of Clarke & Pringle (1988). The motion of the dust particles are influenced by the hydrodynamic drag by the disk gas. Considering dust particles

with finite inertia, their radial velocity (Takeuchi & Lin 2002; Takeuchi & Lin 2005; Zhu et al. 2012) is

$$v_d = \frac{v_g T_S^{-1} - \eta v_K}{T_S + 1/T_S} \quad (6)$$

where $\eta = -h^2 d \ln P / d \ln R$ with $h = H/R$ is a measure for the sub-Keplerian rotation of gas and $v_K = \sqrt{GM/R}$ is the Keplerian velocity. The Stokes number, or dimensionless stopping time in the Epstein regime (e.g. Birnstiel et al. 2010)

$$T_S = \frac{\pi \rho_d s}{2 \Sigma} = 0.0015 \times \left(\frac{s}{1 \text{ mm}} \right) \left(\frac{\rho_d}{1 \text{ g cm}^{-3}} \right) \left(\frac{100 \text{ g cm}^{-2}}{\Sigma} \right), \quad (7)$$

depends on individual dust grains' radius s , internal *physical* density ρ_d , and the gas volume density ρ_g .

In the case of MRI turbulence, the diffusion coefficients measured for the middle plane and surface of the disk are different, and we correspondingly treat the dust distribution as two stratified layers, with the middle plane dust concentrations $C_{\text{mid}}(R, \theta, t) = \int_0^H \rho_d dz / \int_0^H \rho_g dz$ and surface layer concentration $C_{\text{sur}}(R, \theta, t) = \int_H^\infty \rho_d dz / \int_0^H \rho_g dz$ where ρ_g is the gas density and ρ_d is the dust density. Locally if the two layers have different densities, there would be a linear mass transfer rate $\lambda = D_z / H^2$ between the two layers. We can write down the coupled two-layer diffusion problem as

$$\phi \Sigma \frac{\partial C_{\text{mid}}}{\partial t} = \frac{1}{R} \frac{\partial}{\partial R} \left(RD_{\text{mid}} \phi \Sigma \frac{\partial C_{\text{mid}}}{\partial R} \right) - \frac{1}{R} \frac{\partial}{\partial R} (R \phi \Sigma v_{d,\text{mid}} C_{\text{mid}}) + C_{\text{mid}} \frac{1}{R} \frac{\partial}{\partial R} (R \phi \Sigma v_g) + F_z \quad (8)$$

$$(1 - \phi) \Sigma \frac{\partial C_{\text{sur}}}{\partial t} = \frac{1}{R} \frac{\partial}{\partial R} \left(RD_{\text{sur}} (1 - \phi) \Sigma \frac{\partial C_{\text{sur}}}{\partial R} \right) - \frac{1}{R} \frac{\partial}{\partial R} (R (1 - \phi) \Sigma v_{d,\text{sur}} C_{\text{sur}}) + C_{\text{sur}} \frac{1}{R} \frac{\partial}{\partial R} (R (1 - \phi) \Sigma v_g) - F_z \quad (9)$$

where ϕ is the fraction of gas mass in the middle plane. $F_z = \Sigma D_z / H^2 ((1 - \phi) C_{\text{sur}} - \phi C_{\text{mid}})$ is the vertical diffusion term. $v_{d,\text{mid}}$ and $v_{d,\text{sur}}$ are the radial velocity of dust in the mid-plane and surface layer.

For simplicity, we take $\phi = 0.7$ approximating a Gaussian vertical profile, assuming a constant $h = H/R = 0.05$, and therefore $\eta = (1 - d \ln \Sigma / d \ln R) h^2$ and $\nu = \alpha h^2 \sqrt{GM/R} \propto R^{0.5}$.

We choose different α for different turbulence models according to Table 1 unless otherwise specified. The inner boundary is set at a normalizing length scale $R_{\text{in}} =$

1.0 with absorbing boundary condition for the dust concentration $C(R = R_{\text{in}}) = 0$. For the GI-dominated disk as shown in Fig. 8 the inner boundary is absorbing for the gas density $\Sigma(R = R_{\text{in}}) = 0$, while for the other cases presented below we use Dirichlet boundary condition for gas density (to maintain a steady power law). The outer boundary is set at $R_{\text{out}} = 130$ with a Dirichlet boundary condition for the gas density and absorbing condition for the dust concentration(s). The time unit is set to Ω_{in}^{-1} , the Keplerian dynamical timescale at R_{in} . Focusing on sub-mm size to micron size grains,

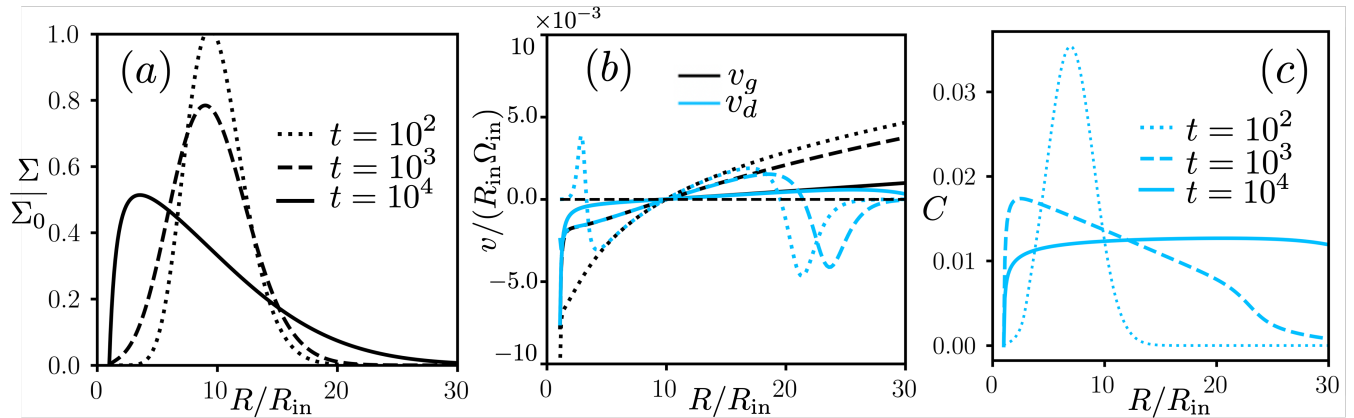


Figure 8. Coupled evolution of gas and dust in an early disk with GI turbulence. The gas density is initialized by a bell curve centered around $R_i = 10$, and it evolves according to Eq. 3, with an absorbing inner boundary. $\alpha = 0.1$, $D_r = 2 H^2 \Omega$. (a) The gas density evolution. (b) the gas drift velocity (black lines) and the dust velocities of the middle plane (blue lines) and the surface layer (red lines). (c) The evolution of dust concentration (blue lines). In all three plots the times are indicated by linestyles: dotted for $t = 100$, dashed for $t = 1000$ and solid for $t = 10000$.

we assume a characteristic dust size corresponding to $T_S = 0.001$, which is well-coupled with gas (see Equation 7) in most of our models with vertically-homogeneous α , neglecting vertical differentiation of dust characteristic size due to sedimentation (Takeuchi & Lin 2003; Garaud et al. 2004). This can be justified by considering the maximum dust Stokes number allowed by fragmentation (Ormel & Cuzzi 2007; Birnstiel et al. 2010; Chen et al. 2020; Li et al. 2019):

$$T_{S,\max} \approx \frac{u_f^2}{2\alpha c_s^2}, \quad (10)$$

for fragmentation velocity $u_f \sim 1\text{m/s}$, typical sound speed $c_s \sim 1\text{km/s}$ and $\alpha > 0.02$, the characteristic dust species' size growth by coagulation will be halted at T_S smaller than a few 0.001, even in the midplane. Because these dust species already couple fairly well with dust, the diffusion of μm crystalline grains with even smaller T_S will be even better coupled to gas. We will discuss possible effects of having a dead zone with much smaller midplane turbulence in §4.3, where characteristic dust species may be allowed to grow to larger than mm-size.

In the following sections we apply one- and two-layered diffusion model to PSDs at different stages of evolution with the dust diffusion parameter extracted from the turbulence simulations as summarised in Table 1.

4.1. Coupled dust-gas evolution in a gravitationally unstable disk

As the PSD evolves in time, the disk mass and accretion rate gradually decline, regions of gravitational instability will recede and MRI turbulence will dominate in the inner disk (Nakamoto & Nakagawa 1994; Hueso

& Guillot 2005). We first examine the coupled evolution of dust and gas densities in the youngest GI-dominated disks (Xu 2022), by solving Equations 2 and 3 for a homogeneous layer of dust with $T_s = 0.001$, using $\alpha = 0.1$ and $D_r = 2$. Considering the early disk to be very dynamic and GI dominated, we demonstrate an initially bell-shaped gas density using a Gamma distribution, as shown in Figure 8(a)

$$\Sigma(R) = \Sigma_0 \frac{6(R - R_{\text{in}})^{k-1} e^{-(R - R_{\text{in}})/\theta}}{\Gamma(k)\theta^k} \quad (11)$$

where $k = 15$ and $\theta = 0.6$ are the shape parameters and Σ_0 is the gas surface density unit. The gas density evolution induces a separatrix around the peak of the initial distribution $R_{\text{peak}} \sim 10$, where gas drift velocity is inward for $R < R_{\text{peak}}$ and outward for $R > R_{\text{peak}}$, as seen in Figure 8(b). The factor 6 is chosen such that the peak value of gas density is $\approx \Sigma_0$. For the initial dust density, we choose a narrow ring around an arbitrary radius $R_0 = 8$ analogous to the delta function adopted by Clarke & Pringle (1988). After 10000 dynamical timescales at the inner boundary, significant outward/upstream diffusion of the dust concentration is seen in Figure 8(c). By the end of the simulation (solid lines), both the gas and dust density profiles have significantly flattened, while the gas and dust advection velocities have coupled with each other, conserving the location of the velocity separatrix. Due to large values of $D_r = 2.0$, a considerable portion of grains can diffuse out to $R \gg R_0$ although its peak will still drift towards the inner boundary at velocities close to v_g , which is negative for $R \lesssim R_{\text{peak}}$.

At a later stage, significant GI and MHD turbulence co-exist to influence disk evolution. Reading off Table 1, we apply viscosity coefficient $\alpha = 0.2$ and radial diffusion

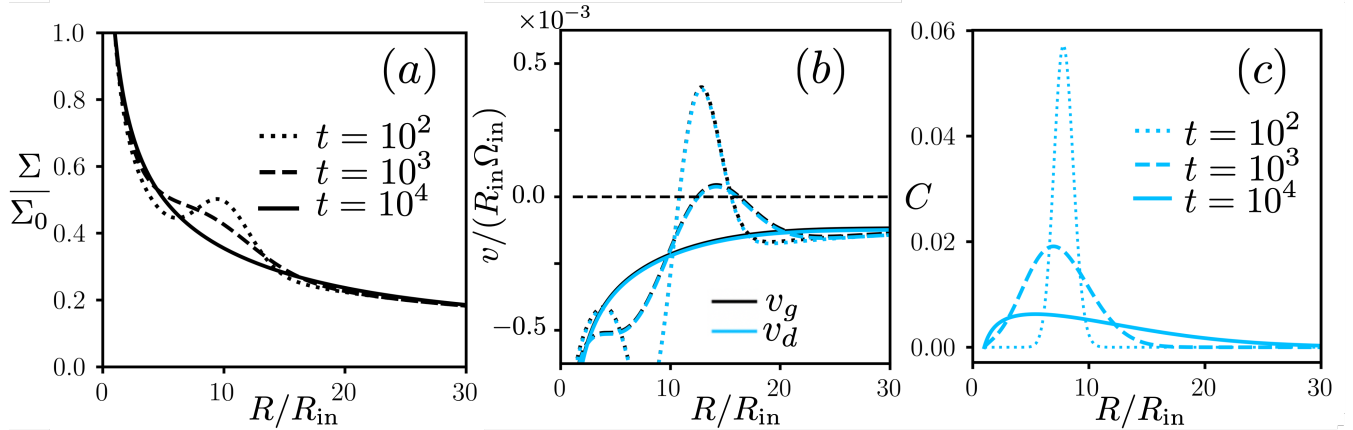


Figure 9. Coupled evolution of gas and dust in a GI-MHD disk perturbed from the steady-state power-law distribution. $\alpha = 0.2$, $D_r = 0.5 H^2 \Omega$. (a) The gas density evolution and (b) the gas drift velocity (black lines) and the dust velocity (blue lines) almost overlap throughout the evolution, due to small grain sizes with $T_S = 0.001$. (c) The evolution of dust/gas ratio from solving Equations 2 and 3. In all three plots the times are indicated by linestyles: dotted for $t = 100$, dashed for $t = 1000$ and solid for $t = 10000$.

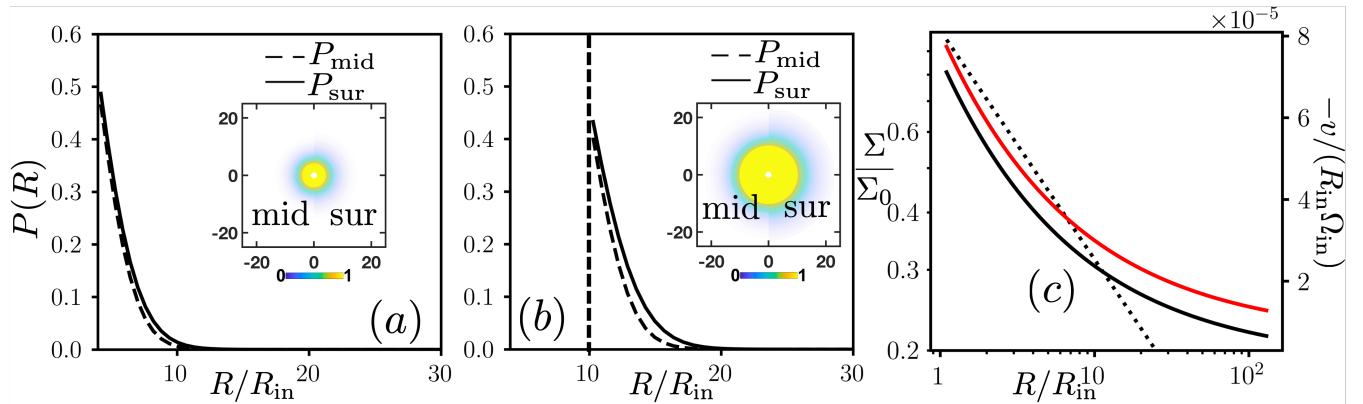


Figure 10. The maximum upstream fractions $P(R)$ (dimensionless) at $t = 1 \times 10^4 \Omega_{\text{in}}^{-1}$, due to ideal MRI turbulence, computed for the initial dust ring positioned at (a) $R_0 = 4$ and (b) $R_0 = 10$ with $\alpha = 0.02$, $D_{\text{mid}} = 0.033 H^2 \Omega$, $D_{\text{sur}} = 0.07 H^2 \Omega$, $D_z = 0.013 H^2 \Omega$. $T_{S,\text{mid}} = T_{S,\text{sur}} = 0.001$. Solid lines represent the surface layer, and dashed lines are for the middle plane layer. The inset shows the inferred disk concentration images, with the left half representing the middle plane layer and the right half representing the surface layer. (c) The steady state power-law gas density (dotted black line, label on the left), gas radial velocity (black solid line) and the dust radial drag velocity (red line, label on the right).

coefficient $D_r = 0.5$. We find that the Bell curve initial condition (Equation 11) follows a similar diffusion process, only slower in time by a factor of 3-4 due to change in D_r . To mimic a relatively more stable disk profile, we then consider another initial gas density by superimposing a Gaussian bump on a steady-state power-law. The gas bump is also centered at around $R_{\text{peak}} = 10$.

$$\Sigma = \Sigma_0 R^{-0.5} + 0.2 \Sigma_0 e^{-\frac{(R-R_{\text{peak}})^2}{2\sigma_g^2}} \quad (12)$$

with the Gaussian spread chosen as $\sigma_g = 2.0$, as shown in Figure. 9(a) with dotted lines. The gas/dust radial velocities are shown in Figure 9(b), and the typical dust concentrations at times $t = 100, 1000, 10000$ are shown in Figure 9(c). Throughout the simulation, the dust

and gas velocities are tightly coupled with each other. At the end of the simulation, the gas density relaxes towards a power law, and the dust concentration always spread out beyond the initial ring position R_0 , although its peak still migrates inward due to a generally negative advection velocity profile. For GI-MHD turbulence we also tried to start with a smooth steady-state gas profile without the Gaussian bump (with $v_d \approx v_g$ being negative throughout the simulation), and found the evolution of dust concentration is very similar to Figure 9(c), confirming that outward radial transport is dominated by diffusion rather than advection as $D_r > \alpha$.

4.2. Upstream diffusion of dust in a steady-state MRI disk with ideal MHD turbulence

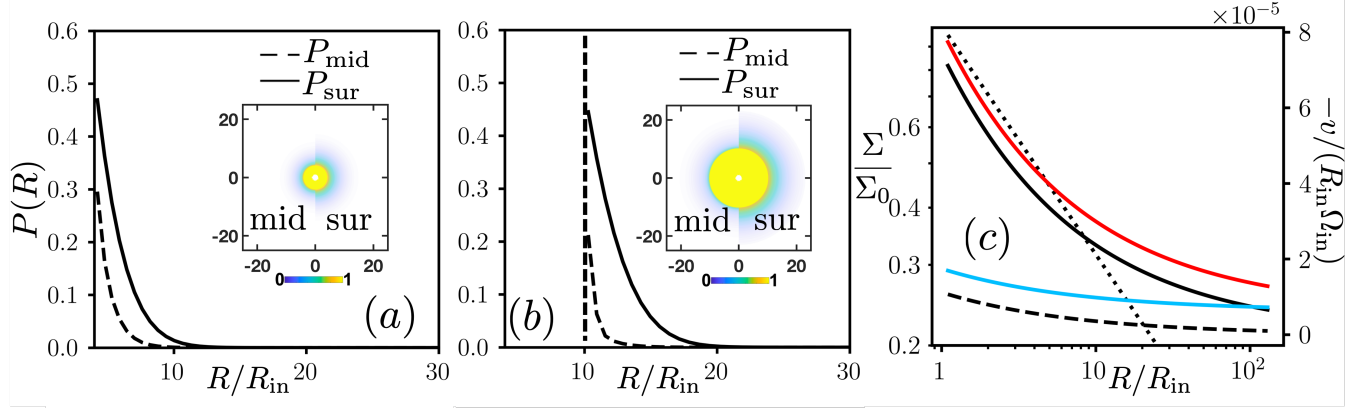


Figure 11. The maximum upstream fractions $P(R)$ at $t = 1 \times 10^4 \Omega_{\text{in}}^{-1}$, due to non-ideal MRI turbulence, computed for the initial dust ring positioned at (a) $R_0 = 4$ and (b) $R_0 = 10$ with $\alpha_{\text{mid}} = 0.003$, $\alpha_{\text{sur}} = 0.02$, $D_{\text{mid}} = D_z = 0.003 H^2\Omega$, $D_{\text{sur}} = 0.07 H^2\Omega$. $T_{\text{S,mid}} = T_{\text{S,sur}} = 0.001$. Solid lines represent the surface layer, and dashed lines are for the middle plane layer. The inset shows the inferred disk concentration images, with the left half representing the middle plane layer and the right half representing the surface layer. (c) The steady state power-law gas density (dotted black line), gas radial velocities of the middle plane (dashed black line) and the surface layer (solid black line), and the dust radial drag velocities of the middle plane (blue line) and the surface layer (red line).

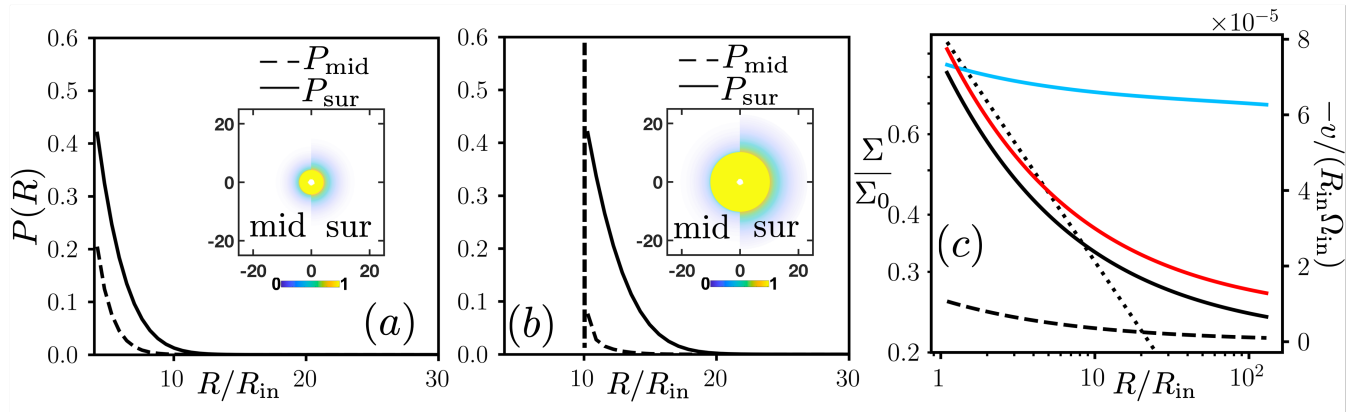


Figure 12. The maximum upstream fractions $P(R)$ at $t = 1 \times 10^4 \Omega_{\text{in}}^{-1}$, due to non-ideal MRI turbulence and differential stopping times, computed for the initial dust ring positioned at (a) $R_0 = 4$ and (b) $R_0 = 10$ with $\alpha_{\text{sur}} = 0.02$, $\alpha_{\text{mid}} = 0.003$, $D_{\text{sur}} = 0.07 H^2\Omega$, $D_{\text{mid}} = D_z = 0.003 H^2\Omega$. The stopping times are chosen as $T_{\text{S,mid}} = 0.01$, $T_{\text{S,sur}} = 0.001$. Solid lines represent the surface layer, and dashed lines are for the middle plane layer. The inset shows the inferred disk concentration images, with the left half representing the middle plane layer and the right half representing the surface layer. (c) The steady state power-law gas density (dotted black line), gas radial velocities of the middle plane (dashed black line) and the surface layer (solid black line), and the dust radial drag velocities of the middle plane (blue line) and the surface layer (red line).

For quasi-steady MRI turbulence applicable to a later stage of PSD evolution, in the simulation we measure a radial accretion flow with a velocity $\sim -10^{-4}v_K$. With $H/R \lesssim 0.1$ and $\alpha \sim 2 \times 10^{-2}$, this value is on the order of the radial velocity in the steady solution (e.g. [Clarke & Pringle 1988](#))

$$v_g = -\frac{3\nu}{2R}. \quad (13)$$

Here we examine dust evolution also based on the steady-state model for gas accretion flow. We demonstrate the possibility of upstream diffusion with the corresponding steady-state $\Sigma = \Sigma_0 R^{-0.5}$ profile. Since

the gas evolution equation gives $\partial\Sigma/\partial t = 0$, we only solve the dust evolution equations, but we distinguish two layers of dust with different radial diffusion coefficients $D_{\text{mid}} = 0.033$ and $D_{\text{sur}} = 0.07$ from Table 1. We further apply $\alpha = 0.02$ and make use of $D_z = 0.013$. The dust evolution is then solved using Equations 8 & 9, neglecting feedback on the gas profile, where initially a ring of dust with $T_S = 0.001$ is located at R_0 . The F_z term represents vertical diffusion between two layers. The time-independent gas density (black) and the radial advection velocities (red) are shown in Figure 10(c). To quantify the extent of outward grain diffusion

in our MHD case and better compare two layers, instead of directly showing the radial evolution of C , which is much more quiescent than Figure 8(c) and Figure 9(c), we compute the maximum fraction of dust mass that reaches the region $R > R_0$ beyond the initial radial location of the dust ring, defined as

$$P_i(R) = \max_{0 < t < T} \frac{\int_R^\infty 2\pi R \Sigma C_i dR}{\int_{R_{\text{in}}}^\infty 2\pi R \Sigma C_i dR} \quad (14)$$

where $R_{\text{in}} = 1.0$ is taken as the position of the inner absorbing boundary, $T = 1 \times 10^4 \Omega^{-1}$ the total simulation time, and $i = \text{mid, sur}$ for the midplane layer and surface layer respectively. Figure 10(a)(b) show the maximum fractions of dust mass reaching different radius $R > R_0$, for two typical values of $R_0 = 4$ and $R_0 = 10$. The insets of Figure 10(a)(b) show axisymmetric 2D distribution of $P(R)$ from the upstream fraction curves. In both cases, the surface layer display stronger upstream diffusion compared to the middle plane due to an order-unity larger D_{sur} , although the midplane dust can also diffuse outwards significantly in the ideal MHD setup.

4.3. Dust evolution in a steady-state MRI disk with non-ideal MHD turbulence

We then consider the effect of non-ideal MHD turbulence, where the midplane of the disk is much less ionized and less coupled to the MRI turbulence (Gammie 1996; Kretke & Lin 2010), with effective $\alpha_{\text{mid}} \sim 10^{-3}$. Hence, the diffusion in the middle plane and the vertical direction may be constrained by α_{mid} and much less effective. We test this effect by going beyond simulation measurements and reducing coefficients to $D_{\text{mid}} = D_z = 0.003$. The midplane layer's v_g and v_d are also reduced according to a smaller $\alpha_{\text{mid}} = 0.003$. In 3D non-ideal MHD simulations, gas in certain regions of the upper layer $|z| \gtrsim H$ can have positive radial velocity, albeit significant outflow ($v_g \sim v_K$) only occurs at $|z| \gg H$ where gas density is negligible (Bai 2017). In our 2D treatment we still make the simplification to match a characteristic negative v_g of the MRI-active layer with the inward accretion rate to ensure steady-state (Gammie 1996), proportional to the characteristic α that we assume in that layer. Note that if our upper layer has a significant positive gas velocity, dust outward transport will be aided by a combination of outward advection and diffusion, which will appear even more significant. Nevertheless, currently we only focus on the effect of the latter. The results are presented in Figure 11 similar to Figure 10. The midplane now shows much smaller upstream fractions, as seen in (a)(b). The gas inflow velocity is much larger near the surface than the midplane, due to $\alpha_{\text{sur}} \gg \alpha_{\text{mid}}$, and the dust inward-drift

speed near the surface is also faster than that in the mid-plane (c). Nevertheless, upstream diffusion is much more pronounced near the surface than the mid-plane, due to $D_{\text{sur}} \gg D_{\text{mid}}$.

Additionally, we consider the dust sizes in the midplane being larger (super-mm) than the surface layer (sub-mm or micron) due to relaxation of the fragmentation barrier (Equation 10), producing a larger characteristic Stokes number for the midplane characteristic dust species $T_{s,\text{mid}} = 0.01$. Results from this setup is shown in Figure 12. The difference in dust velocities for the two layers are significantly enhanced, as seen in Figure 12(c), while segregation effect becomes stronger and the surface layer can diffuse upstream significantly while the midplane is dominated by slow inward radial drift, as seen in Figure 12 (a) and (b). Changing the stopping time for mid-plane layer to $T_{s,\text{mid}} = 0.1$ could enhance this segregation effect even further.

4.4. Dust evolution in an ideal MRI disk with stellar radiation wind

At the final stages of gaseous disk evolution, accretion heating becomes subdominant and the central star illuminates the outer disk (Nakamoto & Nakagawa 1994; Hueso & Guillot 2005), which could cause significant evaporation of the gas density (Takeuchi & Lin 2003). To study the sole effect of radiation wind, based on the ideal MHD model (§4.2), we modify Equation 3 to include a sink term

$$\frac{\partial \Sigma}{\partial t} = \frac{3}{R} \frac{\partial}{\partial R} \left(R^{1/2} \frac{\partial}{\partial R} (\Sigma \nu R^{1/2}) \right) - \frac{\Sigma}{\tau_{\text{wind}}} f(R) \quad (15)$$

where $f(R) = (\tanh[(R - R_w)/\sigma_w] + 1)/2$ is a smoothing function.

We solve the modified gas evolution equation together with Equations 8 and 9, choosing fiducial parameters within a range around $\tau_{\text{wind}} \sim 100$, $R_w \sim 15$ and $\sigma_w \sim 5$. All other parameters are similar to that of Figure 10. The reduction of gas density beyond R_w induces an outward gas velocity, on the same order of magnitude as the steady-state inward gas velocity. The resulting dust evolution is similar to the ideal MHD case presented in Figure 10, and both the surface layer and middle plane show considerable upstream diffusion.

5. SUMMARY

Based on measurements from numerical simulations, we constructed 1D accretion disk models of gas and dust to determine outcomes of long-term diffusion process. In the simulations, we separate the disk into the midplane $|z| \lesssim H$ section and the surface section $|z| \gtrsim H$. Characteristic radial diffusion coefficients for each layer

D_{mid} and D_{sur} are measured from Lagrangian particle diffusion, while exchange of particles between two layers is controlled by an overall vertical diffusion coefficient D_z . In the GI and GI-MHD runs, we found $D_z \sim \alpha \sim 0.1 - 0.2$ is quite efficient and the radial diffusion has little vertical dependence $D_{mid} \approx D_{sur} \sim D_r$, therefore in §4.1 we only consider one homogeneous layer of μm size dust with characteristic Stokes number $T_s = 0.001$. The early stage of a PSD is GI or GI-MHD dominated and highly dynamical, therefore we apply impulsive initial conditions with an evolving gas profile. We found very efficient diffusion of dust with $T_S \lesssim 0.001$ due to D_r much larger than the gas accretion coefficient α . This implies that not only micron-size crystalline (highly refractory) grains condensed interior to the main belt of asteroid region can be transported outwards to Heliocentric distance of the Kuiper Belt region and be incorporated into comets (such as those retrieved from comet 81P Wild 2 by the Stardust mission), but up to mm-size CAI condensed in the sub-au inner regions are also prone to marginal gravitational instability, and can spread out to the super-au main-belt regions to be assimilated into the planetesimal parent bodies of chondritic meteorites.

At a later stage, we consider a relatively quiescent MRI dominated disk with a fixed density profile; We first apply a diffusion model with two layers of dust of different diffusion coefficient $D_{sur} > D_{mid}$ according to the MHD simulation. Although diffusion coefficients are much smaller than in the gravito-turbulence

case, we still observe upstream diffusion of dust in both layers. That is to say, a considerable fraction of dust may reach the region beyond a its initial radial location through the effect of concentration diffusion. While the difference between two layers is small for our ideal-MHD model (§4.2), we also explore the influence of the existence of dead zone (§4.3), where the turbulence parameter α is significantly smaller and characteristic dust Stokes number $T_{S,mid}$ can be significantly larger than the surface layer $T_{S,sur}$. In this case, the upstream diffusion of mm or cm grains in the dead zone is much less vigorous than grains in the surface. This effect attributes to the difference in disk radii inferred from NIR emission by mm-size dust in the midplane, or scattered light by micron-size grains near the disk surface (Villenave et al. 2020; Benisty et al. 2022). We lastly consider photo-evaporating winds in the outer regions of the disk, and found its sole effect can mildly enhance the upstream diffusion, albeit its efficiency is limited.

- 1 We thank William Bethune, Hans Baehr, Zhaohuan Zhu
- 2 and Wenrui Xu for useful conversations. We thank the
- 3 anonymous referee for helpful suggestions. We have ben-
- 4 efitated from many past discussions with Willy Kley and
- 5 would like to dedicate this paper to his memory. Y.
- 6 X. C. thanks Man Hoi Lee and Hong Kong Univer-
- 7 sity for their hospitality during the completion of this
- 8 manuscript. T.Z. is supported by the Cecil and Sally
- 9 Drinkward postdoc fellowship during this work.

REFERENCES

- Adams, F. C., Lada, C. J., & Shu, F. H. 1987, *ApJ*, 312, 788, doi: [10.1086/164924](https://doi.org/10.1086/164924)
- Armitage, P. J. 2019, in *From Protoplanetary Disks to Planet Formation* (Springer), 1–150
- Baehr, H., & Zhu, Z. 2021, *ApJ*, 909, 136, doi: [10.3847/1538-4357/abddb4](https://doi.org/10.3847/1538-4357/abddb4)
- Bai, X.-N. 2017, *ApJ*, 845, 75, doi: [10.3847/1538-4357/aa7dda](https://doi.org/10.3847/1538-4357/aa7dda)
- Bai, X.-N., & Stone, J. M. 2013, *The Astrophysical Journal*, 769, 76
- Balbus, S. A., & Hawley, J. F. 1991, *ApJ*, 376, 214, doi: [10.1086/170270](https://doi.org/10.1086/170270)
- . 1998, *Reviews of Modern Physics*, 70, 1, doi: [10.1103/RevModPhys.70.1](https://doi.org/10.1103/RevModPhys.70.1)
- Beckwith, K., Armitage, P. J., & Simon, J. B. 2011, *Monthly Notices of the Royal Astronomical Society*, 416, 361
- Benisty, M., Dominik, C., Follette, K., et al. 2022, arXiv preprint arXiv:2203.09991
- Béthune, W., Latter, H., & Kley, W. 2021, *Astronomy & Astrophysics*, 650, A49
- Birnstiel, T., Dullemond, C. P., & Brauer, F. 2010, *A&A*, 513, A79, doi: [10.1051/0004-6361/200913731](https://doi.org/10.1051/0004-6361/200913731)
- Bockelée-Morvan, D., Gautier, D., Hersant, F., Huré, J. M., & Robert, F. 2002, *A&A*, 384, 1107, doi: [10.1051/0004-6361:20020086](https://doi.org/10.1051/0004-6361:20020086)
- Boley, A., & Durisen, R. 2006, *The Astrophysical Journal*, 641, 534
- Boley, A. C., & Durisen, R. H. 2010, *The Astrophysical Journal*, 724, 618
- Bouwman, J., de Koter, A., Dominik, C., & Waters, L. B. F. M. 2003, *A&A*, 401, 577, doi: [10.1051/0004-6361:20030043](https://doi.org/10.1051/0004-6361:20030043)
- Bouwman, J., Henning, T., Hillenbrand, L. A., et al. 2008, *ApJ*, 683, 479, doi: [10.1086/587793](https://doi.org/10.1086/587793)

- Brownlee, D., Tsou, P., Aléon, J., et al. 2006, *Science*, 314, 1711, doi: [10.1126/science.1135840](https://doi.org/10.1126/science.1135840)
- Cameron, A. G. W. 1978, *Moon and Planets*, 18, 5, doi: [10.1007/BF00896696](https://doi.org/10.1007/BF00896696)
- Chen, Y.-X., Li, Y.-P., Li, H., & Lin, D. N. C. 2020, *ApJ*, 896, 135, doi: [10.3847/1538-4357/ab9604](https://doi.org/10.3847/1538-4357/ab9604)
- Chen, Y.-X., Wang, Z., Li, Y.-P., Baruteau, C., & Lin, D. N. C. 2021, *ApJ*, 922, 184, doi: [10.3847/1538-4357/ac23d7](https://doi.org/10.3847/1538-4357/ac23d7)
- Chiang, E. I., & Goldreich, P. 1997, *ApJ*, 490, 368, doi: [10.1086/304869](https://doi.org/10.1086/304869)
- Ciesla, F. J. 2007, *Science*, 318, 613, doi: [10.1126/science.1147273](https://doi.org/10.1126/science.1147273)
- Clarke, C. J. 1989, *MNRAS*, 238, 283, doi: [10.1093/mnras/238.2.283](https://doi.org/10.1093/mnras/238.2.283)
- Clarke, C. J., & Pringle, J. E. 1988, *MNRAS*, 235, 365, doi: [10.1093/mnras/235.2.365](https://doi.org/10.1093/mnras/235.2.365)
- Colbrook, M. J., Ma, X., Hopkins, P. F., & Squire, J. 2017, *MNRAS*, 467, 2421, doi: [10.1093/mnras/stx261](https://doi.org/10.1093/mnras/stx261)
- Deng, H., Mayer, L., & Helled, R. 2021, *Nature Astronomy*, 5, 440
- Deng, H., Mayer, L., & Latter, H. 2020, *The Astrophysical Journal*, 891, 154
- Deng, H., Mayer, L., Latter, H., Hopkins, P. F., & Bai, X.-N. 2019, *The Astrophysical Journal Supplement Series*, 241, 26
- Deng, H., Mayer, L., & Meru, F. 2017, *The Astrophysical Journal*, 847, 43
- Desch, S. J., Morris, M. A., Connolly, H. C., & Boss, A. P. 2012, *M&PS*, 47, 1139, doi: [10.1111/j.1945-5100.2012.01357.x](https://doi.org/10.1111/j.1945-5100.2012.01357.x)
- Durisen, R. H., Boss, A. P., Mayer, L., et al. 2007, in *Protostars and Planets V*, ed. B. Reipurth, D. Jewitt, & K. Keil, 607. <https://arxiv.org/abs/astro-ph/0603179>
- Gammie, C. F. 1996, *ApJ*, 457, 355, doi: [10.1086/176735](https://doi.org/10.1086/176735)
- Garaud, P., Barrière-Fouchet, L., & Lin, D. N. C. 2004, *ApJ*, 603, 292, doi: [10.1086/381385](https://doi.org/10.1086/381385)
- Garaud, P., & Lin, D. N. C. 2007, *ApJ*, 654, 606, doi: [10.1086/509041](https://doi.org/10.1086/509041)
- Gong, M., Zheng, X., Lin, D. N. C., et al. 2019, *ApJ*, 883, 164, doi: [10.3847/1538-4357/ab3e70](https://doi.org/10.3847/1538-4357/ab3e70)
- Haghighipour, N., & Boss, A. P. 2003, *The Astrophysical Journal*, 583, 996
- Hartmann, L. 1998, *Accretion Processes in Star Formation*
- Hayashi, C., Nakazawa, K., & Nakagawa, Y. 1985, in *Protostars and Planets II*, ed. D. C. Black & M. S. Matthews, 1100–1153
- Hopkins, P. F. 2015, *Monthly Notices of the Royal Astronomical Society*, 450, 53
- Hu, Z., & Bai, X.-N. 2021, *MNRAS*, 503, 162, doi: [10.1093/mnras/stab542](https://doi.org/10.1093/mnras/stab542)
- Hueso, R., & Guillot, T. 2005, *A&A*, 442, 703, doi: [10.1051/0004-6361:20041905](https://doi.org/10.1051/0004-6361:20041905)
- Ida, S., & Lin, D. N. C. 2004, *ApJ*, 604, 388, doi: [10.1086/381724](https://doi.org/10.1086/381724)
- Kley, W., & Lin, D. N. C. 1992, *ApJ*, 397, 600, doi: [10.1086/171818](https://doi.org/10.1086/171818)
- Kratter, K., & Lodato, G. 2016, *Annual Review of Astronomy and Astrophysics*, 54, 271
- Kretke, K. A., & Lin, D. 2010, *The Astrophysical Journal*, 721, 1585
- Krumholz, M. R., Burkhardt, B., Forbes, J. C., & Crocker, R. M. 2018, *MNRAS*, 477, 2716, doi: [10.1093/mnras/sty852](https://doi.org/10.1093/mnras/sty852)
- Li, Y.-P., Li, H., Ricci, L., et al. 2019, *ApJ*, 878, 39, doi: [10.3847/1538-4357/ab1ff6](https://doi.org/10.3847/1538-4357/ab1ff6)
- Lin, D. N. C., & Papaloizou, J. 1985, in *Protostars and Planets II*, ed. D. C. Black & M. S. Matthews, 981–1072
- Liu, B., Johansen, A., Lambrechts, M., Bizzarro, M., & Haugbølle, T. 2022, *Science Advances*, 8, eabm3045, doi: [10.1126/sciadv.abm3045](https://doi.org/10.1126/sciadv.abm3045)
- Löhnert, L., & Peeters, A. 2022
- Lynden-Bell, D., & Pringle, J. E. 1974, *MNRAS*, 168, 603, doi: [10.1093/mnras/168.3.603](https://doi.org/10.1093/mnras/168.3.603)
- Morfill, G. E., & Voelk, H. J. 1984, *ApJ*, 287, 371, doi: [10.1086/162697](https://doi.org/10.1086/162697)
- Nakamoto, T., & Nakagawa, Y. 1994, *ApJ*, 421, 640, doi: [10.1086/173678](https://doi.org/10.1086/173678)
- Ogilvie, G. I. 2018, *Monthly Notices of the Royal Astronomical Society*, 477, 1744
- Okuzumi, S., & Hirose, S. 2011, *The Astrophysical Journal*, 742, 65
- Ormel, C. W., & Cuzzi, J. N. 2007, *A&A*, 466, 413, doi: [10.1051/0004-6361:20066899](https://doi.org/10.1051/0004-6361:20066899)
- Pringle, J. E. 1981, *ARA&A*, 19, 137, doi: [10.1146/annurev.aa.19.090181.001033](https://doi.org/10.1146/annurev.aa.19.090181.001033)
- Rice, W., Lodato, G., Pringle, J., Armitage, P., & Bonnell, I. A. 2004, *Monthly Notices of the Royal Astronomical Society*, 355, 543
- Riols, A., & Latter, H. 2019, *Monthly Notices of the Royal Astronomical Society*, 482, 3989
- Riols, A., Lesur, G., & Menard, F. 2020a, *Astronomy & Astrophysics*, 639, A95
- Riols, A., Roux, B., Latter, H., & Lesur, G. 2020b, *Monthly Notices of the Royal Astronomical Society*, 493, 4631
- Ruden, S. P., & Lin, D. N. C. 1986, *ApJ*, 308, 883, doi: [10.1086/164559](https://doi.org/10.1086/164559)
- Safronov, V. S. 1960, *Annales d’Astrophysique*, 23, 979

- Safronov, V. S., & Ruzmaikina, T. V. 1985, in *Protostars and Planets II*, ed. D. C. Black & M. S. Matthews, 959–980
- Shakura, N. I., & Sunyaev, R. A. 1973, *A&A*, 24, 337
- Shang, H., Shu, F. H., Lee, T., & Glassgold, A. E. 2000, *SSRv*, 92, 153, doi: [10.1023/A:1005234909848](https://doi.org/10.1023/A:1005234909848)
- Shi, J.-M., Zhu, Z., Stone, J. M., & Chiang, E. 2016, *MNRAS*, 459, 982, doi: [10.1093/mnras/stw692](https://doi.org/10.1093/mnras/stw692)
- Shu, F. H., Najita, J. R., Shang, H., & Li, Z. Y. 2000, in *Protostars and Planets IV*, ed. V. Mannings, A. P. Boss, & S. S. Russell, 789–814
- Shu, F. H., Shang, H., Gounelle, M., Glassgold, A. E., & Lee, T. 2001, *ApJ*, 548, 1029, doi: [10.1086/319018](https://doi.org/10.1086/319018)
- Simon, J. B., Beckwith, K., & Armitage, P. J. 2012, *Monthly Notices of the Royal Astronomical Society*, 422, 2685
- Takeuchi, T., & Lin, D. 2005, *The Astrophysical Journal*, 623, 482
- Takeuchi, T., & Lin, D. N. C. 2002, *ApJ*, 581, 1344, doi: [10.1086/344437](https://doi.org/10.1086/344437)
- . 2003, *ApJ*, 593, 524, doi: [10.1086/376496](https://doi.org/10.1086/376496)
- Toomre, A. 1964, *The Astrophysical Journal*, 139, 1217
- Urpin, V. A. 1984, *Soviet Ast.*, 28, 50
- van Boekel, R., Min, M., Waters, L. B. F. M., et al. 2005, *A&A*, 437, 189, doi: [10.1051/0004-6361:20042339](https://doi.org/10.1051/0004-6361:20042339)
- Villenave, M., Ménard, F., Dent, W., et al. 2020, *Astronomy & Astrophysics*, 642, A164
- Watson, D. M., Leisenring, J. M., Furlan, E., et al. 2009, *ApJS*, 180, 84, doi: [10.1088/0067-0049/180/1/84](https://doi.org/10.1088/0067-0049/180/1/84)
- Weidenschilling, S. J., Marzari, F., & Hood, L. L. 1998, *Science*, 279, 681, doi: [10.1126/science.279.5351.681](https://doi.org/10.1126/science.279.5351.681)
- Wissing, R., Shen, S., Wadsley, J., & Quinn, T. 2022, *Astronomy & Astrophysics*, 659, A91
- Wooden, D., Desch, S., Harker, D., Gail, H. P., & Keller, L. 2007, in *Protostars and Planets V*, ed. B. Reipurth, D. Jewitt, & K. Keil, 815
- Xu, W. 2022, *ApJ*, 934, 156, doi: [10.3847/1538-4357/ac7b94](https://doi.org/10.3847/1538-4357/ac7b94)
- Yang, C.-C., & Krumholz, M. 2012, *ApJ*, 758, 48, doi: [10.1088/0004-637X/758/1/48](https://doi.org/10.1088/0004-637X/758/1/48)
- Youdin, A. N., & Lithwick, Y. 2007, *Icarus*, 192, 588, doi: [10.1016/j.icarus.2007.07.012](https://doi.org/10.1016/j.icarus.2007.07.012)
- Zhu, Z., Nelson, R. P., Dong, R., Espaillat, C., & Hartmann, L. 2012, *The Astrophysical Journal*, 755, 6
- Zhu, Z., Nelson, R. P., Hartmann, L., Espaillat, C., & Calvet, N. 2011, *ApJ*, 729, 47, doi: [10.1088/0004-637X/729/1/47](https://doi.org/10.1088/0004-637X/729/1/47)
- Zhu, Z., Stone, J. M., & Bai, X.-N. 2015, *The Astrophysical Journal*, 801, 81